



# Suspended micro thermometer for anisotropic thermal transport measurements

G. de Vito<sup>a</sup>, D.M. Koch<sup>a</sup>, G. Raciti<sup>a</sup>, J.M. Sojo-Gordillo<sup>a</sup>, A. Nigro<sup>a</sup>, R. Swami<sup>a</sup>, Y. Kaur<sup>a</sup>, M.Y. Swinkels<sup>a</sup>, W. Huang<sup>a,b</sup>, T. Paul<sup>b</sup>, M. Calame<sup>a,b,c</sup>, I. Zardo<sup>a,c,\*</sup>

<sup>a</sup> University of Basel, Department of Physics, Klingelbergstrasse 82, 4056, Basel, Switzerland

<sup>b</sup> Transport at Nanoscale Interfaces Laboratory, Empa, 8600 Dübendorf, Switzerland

<sup>c</sup> Swiss Nanoscience Institute, University of Basel, 4056 Basel, Switzerland

## ARTICLE INFO

### Keywords:

Non-local measurements

Thermal transport

Resistive thermometry

Phonons

Raman thermometry

Suspended micro-devices

## ABSTRACT

The investigation of heat flow in nanostructures and low-dimensional system is still a challenging task, though it becomes more and more important for an effective thermal management of microdevices. In this work, we present the fabrication and characterization of a device designed to measure the in-plane thermal properties of nanomaterials in multiple directions. Additionally, the device allows to perform electrical and optical measurements simultaneously. This allows to spatially resolve eventual thermal property anisotropies and the correction of measurements by accounting for the contact resistances. The fabrication has no element that is related to the specific nanostructure to be investigated. The presented concept can be extended for other (quasi-) two dimensional systems and other nanostructures. Finally, we validated the accuracy of the device using a 250 nm thick silicon lamella, which serves as a reference system and offers the possibility to explore the impact of a dominant thermal contact resistance. We have used Raman thermometry to calculate the effective lattice temperature of the lamella as a function of the applied temperature on the membranes. We extracted an average interfacial thermal conductance of  $2.4 \pm 0.8 \times 10^4 \text{ W K}^{-1} \text{ m}^{-2}$ .

## 1. Introduction

Nowadays, integrated circuits technology demands new materials for heat dissipation that can improve computing performances and can easily be integrated into standard semiconductor technology. The investigation of materials with particular thermal properties remains challenging because of the complexity of theoretical models and the high variability of thermal-conductivity values due to poor thermal contact between different materials. Therefore, a device capable of measuring heat flow in multiple directions could offer significant benefits for studying two-dimensional materials or 3D architectures. In particular, such a device could extract the physical properties of anisotropic samples. The interest in 2D materials arises for thermoelectric and

photonic applications because of the high thermal conductivity near room temperature [1]. For instance, few-layers graphene is a promising material for photovoltaic solar cells due to its high transparency, quasi-metallic behaviour, and high thermal dissipation. Moreover, few-layers graphene may be employed in 3D electronics as interconnecting layer and lateral heat spreader [1].

The interest in understanding and manipulating the thermal conduction of nanostructures has led to the development of various methods for measuring thermal transport. A type of thermometric technique enabling spatially dependent measurement is scanning thermal microscopy (SThM). This technique is based on the atomic force microscopy principle but adapted to perform thermal imaging [2]. There are different types of SThM depending on the physical principle to mea-

\* Corresponding author.

E-mail addresses: [giulio.devito@unibas.ch](mailto:giulio.devito@unibas.ch) (G. de Vito), [do.koch@unibas.ch](mailto:do.koch@unibas.ch) (D.M. Koch), [grazia.raciti@unibas.ch](mailto:grazia.raciti@unibas.ch) (G. Raciti), [jose.sojo@unibas.ch](mailto:jose.sojo@unibas.ch) (J.M. Sojo-Gordillo), [arianna.nigro@unibas.ch](mailto:arianna.nigro@unibas.ch) (A. Nigro), [rahul.swami@unibas.ch](mailto:rahul.swami@unibas.ch) (R. Swami), [yashpreet.kaur@unibas.ch](mailto:yashpreet.kaur@unibas.ch) (Y. Kaur), [milo.swinkels@gmail.com](mailto:milo.swinkels@gmail.com) (M.Y. Swinkels), [wenhao.huang@empa.ch](mailto:wenhao.huang@empa.ch) (W. Huang), [tathagata.paul@empa.ch](mailto:tathagata.paul@empa.ch) (T. Paul), [michel.calame@empa.ch](mailto:michel.calame@empa.ch) (M. Calame), [ilaria.zardo@unibas.ch](mailto:ilaria.zardo@unibas.ch) (I. Zardo).

URL: <https://nanophononics.physik.unibas.ch/de/> (G. de Vito).

<https://doi.org/10.1016/j.ijheatmasstransfer.2024.125302>

Received 27 July 2023; Received in revised form 19 January 2024; Accepted 6 February 2024

Available online 19 February 2024

0017-9310/© 2024 The Author(s). Published by Elsevier Ltd. This is an open access article under the CC BY license (<http://creativecommons.org/licenses/by/4.0/>).

sure heat flow. One of them is the thermovoltage-based method, which exploits the thermoelectric potential induced by temperature variation in the tip; another one is the resistive-type of SThM, which is based on the temperature coefficient of electrical resistivity of a resistance located at the tip of the SThM [3]. However, the main limitation of this technique is the interfacial thermal resistance between the tip apex and the samples, which varies depending on the sample's material, the surface roughness, the presence of contamination or of native oxide etc. Additionally, each device must be calibrated prior to performing the experiments. Another important limitation arises from the presence of water meniscus at the tip-sample interface, when the measurement is not performed in vacuum. Although, this potentially improves the thermal contact resistance, it is unreproducible and hard to quantify. Furthermore, this technique requires cumbersome sample-preparation and non-trivial data analysis. Despite these limitations, the SThM remains a powerful tool for temperature-mapping and spatial investigation of the heat flow [4].

Another method used to measure the thermal conductivity of nanostructures and to map the temperature of the heat channels is Raman thermometry, which is an opto-thermal method that uses a laser, typically in steady-state, to detect the temperature response of the material of interest ([1], [5], [6], [7], [8], [9]). The size of the laser spot, diffraction-limited, determines the spatial resolution. The temperature resolution is limited by the spectral resolution of the system and the material-characteristic temperature-dependent Raman shift of the optical phonon modes. While SThM has typically higher spatial and temperature resolution, the advantage of Raman thermometry is that it is not affected by thermal contact resistance.

Instead, a thermometric measurement is provided by devices consisting of suspended membranes featuring electric resistors (also called the thermal-bridge), which are made of a dielectric thin slab that supports metallic serpentine [10]. The membranes are located at the centre of the device and are clamped to the substrate through long beams, that isolate the platforms from the environmental temperature. The transducers generate a heat gradient and sense the variation of temperature on the membranes. Ultimately, the sample of interest is placed between the membranes to control precisely the temperature at its boundaries and to measure the heat power generated.

Although electro-thermal devices provide high sensitivity and good signal to noise ratio, they also involve a very challenging fabrication, leading to a time consuming realisation of working devices. A first example of these microelectromechanical systems (MEMS) comes from Kim and co-workers [11] where single carbon nanotubes were characterized. Similar designs were also used to characterize nanowires for thermoelectric applications [12], to investigate the hydrodynamic effect [13], or to study ballistic transport in nanowires ([14], [15], [16]). This type of device was used, e.g., to extract the thermal conductivity of InAs nanowires [17] or the conductivity of silicon nanowires with a varying cross-section [18]. Similar devices were used to study nanoribbons [19]. A variant of these devices consists in integrating nanowires with the dielectric layer using silicon on insulator wafers ([20], [21]) or using stoichiometric silicon nitride [22].

All these devices are designed to generate a heat flow in one direction and, in any case, they lack of the capability to simultaneously detect the thermal properties of an anisotropic sample in multiple directions.

In this paper, we address the problem of anisotropic measurements in thermal transport by fabricating a MEMS device characterized by four suspended membranes featuring metal transducers. The device is compatible with transmission electron microscopy as well as Raman thermometry. Moreover, the four transducers allow to apply a thermal gradient in multiple directions and sensing the temperature variation at the boundaries of the sample, thus enabling us to resolve anisotropies in the material thermal properties. The primary aim of this device is to investigate 2D materials, in particular hexagonal boron nitride (hBN) and graphene, but it could also be employed to measure nanowires or bulk

materials cut in lamellas. In the following, we will describe the fabrication process of this device, the characterization of its performance, and the evaluation of the contact resistance by measuring a silicon lamella.

## 2. Materials and methods

### 2.1. Micro-device fabrication

The device is composed of four suspended membranes connected to the surrounding through long  $\text{SiN}_x$  beams and metal resistors are patterned on top of the membranes to function as heat transducers.

In Fig. 1, the whole process flow for the suspended device is summarized. The fabrication starts with an undoped 2-inch silicon wafer with a 280  $\mu\text{m}$  thickness (step 1). Subsequently, a layer of 270 nm of amorphous  $\text{SiN}_x$  is deposited on both sides using plasma-enhanced chemical vapour deposition (PECVD) in a PlasmaPro 80 PECVD from Oxford Instruments (step 2).  $\text{SiN}_x$  was chosen due to its high mechanical strength, compatibility with semiconductor technology, low thermal conductivity, electrical insulation, and resistance to strong chemical bases. Then, a 0.5  $\mu\text{m}$  of S1805 photoresist (micro resist technology GmbH) was spin-coated prior to a photolithography process using a  $\mu\text{PG}$  101 Laser Writer from Heidelberg instruments (step 3) in order to open the pattern onto the  $\text{SiN}_x$  (step 4) and expose it to dry etching to make a hard mask for the consequent silicon wet-etching (step 5). The etching mask is patterned onto the photoresist, it is developed using the Microposit MF-319 (micro resist technology GmbH) for 1 minute and, subsequently, the sample is loaded into the SI 500 Reactive ion etcher (RIE) of Sentech to remove the exposed  $\text{SiN}_x$ . Fig. 2 displays the third step where the etching mask is developed. In the RIE's chamber a mixture of 40 sccm of  $\text{CF}_4$  with 80 sccm of Ar at 3 Pa of working pressure and an ICP power of 200 W with 30 W of RF power is imposed for 120 sec.

In the fifth step, the sample is immersed in a 20% diluted aqueous solution of  $\geq 98\%$  pure NaOH (Sigma Aldrich), at 80 °C for 4 hours to remove the exposed silicon, until a layer of around 20  $\mu\text{m}$  is left underneath the other side of the wafer. This left-over layer of silicon is of great use to mechanically support the device in the later process steps and also to assist in the transferring of a two-dimensional flake. The wet-etching mask used to expose the  $\text{SiN}_x$  bottom layer, consists of arrays of squares with 20  $\mu\text{m}$  edge length and with an inter-distance of 4  $\mu\text{m}$ . This pattern allows to first etch the squares until silicon profile of a trapezoid is produced along the  $\langle 100 \rangle$  crystallographic direction, then the process must continue etching the  $\langle 111 \rangle$  planes along the 4  $\mu\text{m}$  inter-distance which has a slower etch rate with respect to the  $\langle 100 \rangle$  [23]. Upon completion of the etching, a layer of silicon on the other side of the wafer is guaranteed (Fig. 2c).

Next, the sample is flipped (step 7) and the entire process is conducted on the opposite side of the wafer, not etched by the NaOH. At this point, we fabricate the electrical pads of the device. To accomplish this, a stack of LOR3A (Kayaku A.M.) and S1805 positive photo-resists with an overall thickness of 760 nm is deposited and subsequently exposed using laser lithography (step 8). The former resist has a higher photon sensitivity with respect to the latter and their combination provides an undercut profile upon laser exposure. This allows precise patterning and a better yield of the metal lift-off, enabling the creation of detailed structures for electrical pads on the wafer surface. Subsequently, thin films of chromium (Cr) and gold (Au) are evaporated with the thicknesses of 5 nm and 75 nm, respectively, using electron beam evaporator Sharon EE-3.

The lift-off process (step 10) consists of dipping the wafer in a bath of Dimethyl Sulfoxide (DMSO, Sigma Aldrich) at 50 °C for one hour, so that the resist with the exceeding metal is removed. Following the Cr/Au lift-off, a layer of 200 nm of Polymethylmethacrylat (PMMA, Kayaku A.M.) is spin-coated on the surface (step 11) and an electron beam lithography (EBL) process using a Zeiss Gemini Supra 35 with Raith Elphy Plus system (step 12) is performed to pattern the heat transducers. Subsequently, a 3 nm and 48 nm thick layers of Cr and

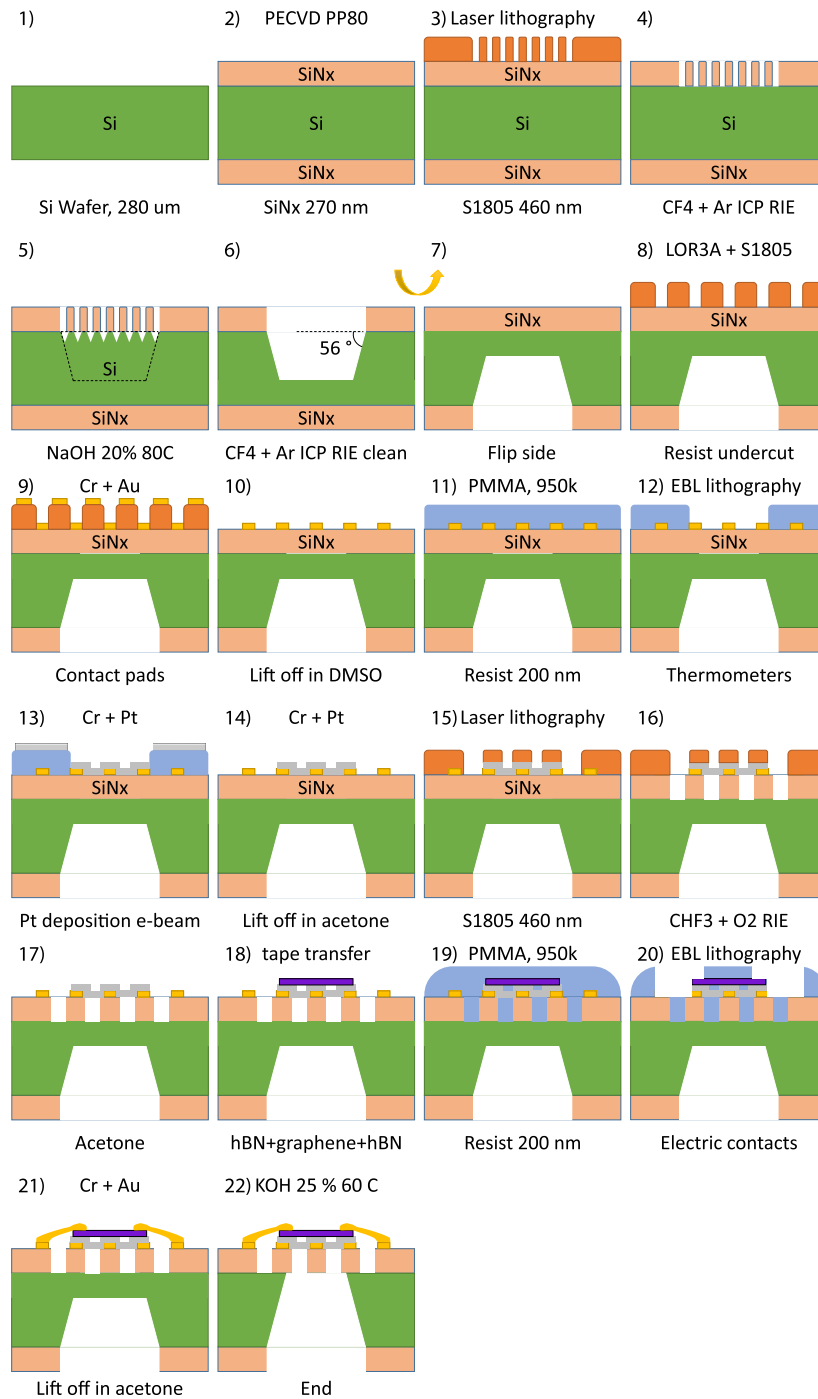


**Fig. 1. Fabrication process flow.** The process flow of the device is displayed. All the schematics are not in scale.

Pt respectively, are deposited by metal evaporation (step 13), then the exceeding PMMA is removed by an acetone bath (step 14). Fig. 3 shows the second Cr/Pt lift-off.

At the fifteenth step, we perform another photolithography to precisely define the shapes of beams and membranes of the SiN<sub>x</sub> layer using a dry etching. The layer is removed by a PLASMALAB 80 plus RIE (Oxford Instruments) using a mixture of 40 sccm of CHF<sub>3</sub> and 8 sccm of O<sub>2</sub> at a working pressure of 60 mTorr and RF power of 60 W (Fig. 3). Following that, the flakes of interest are transferred onto the device using the scotch-tape method (step 18), which consists of picking a flake from the substrate using a glass slide with a layer of Poly(Bisphenol A carbonate) (PC) on top of a slab of Polydimethylsiloxane (PDMS). Af-

ter the flake is picked up by the PC layer, it is aligned with the device centre and subsequently put in contact with the target surface. The PC polymer is melted by heating up the substrate up to 180 °C, so that it can be separated from the slab and then removed by a solution of chloroform. Details of the transferring procedure are described elsewhere [24].

Once the layer is transferred onto the device, we deposit a layer of PMMA (step 19) prior to perform an EBL process (step 20) to deposit the metal contact onto the flake so that it can be electrically characterized. This step leads to clamping the flake firmly onto the surface. Namely, besides providing better thermal contact with the device, the metal deposition is essential to sustain the next step, which consists of

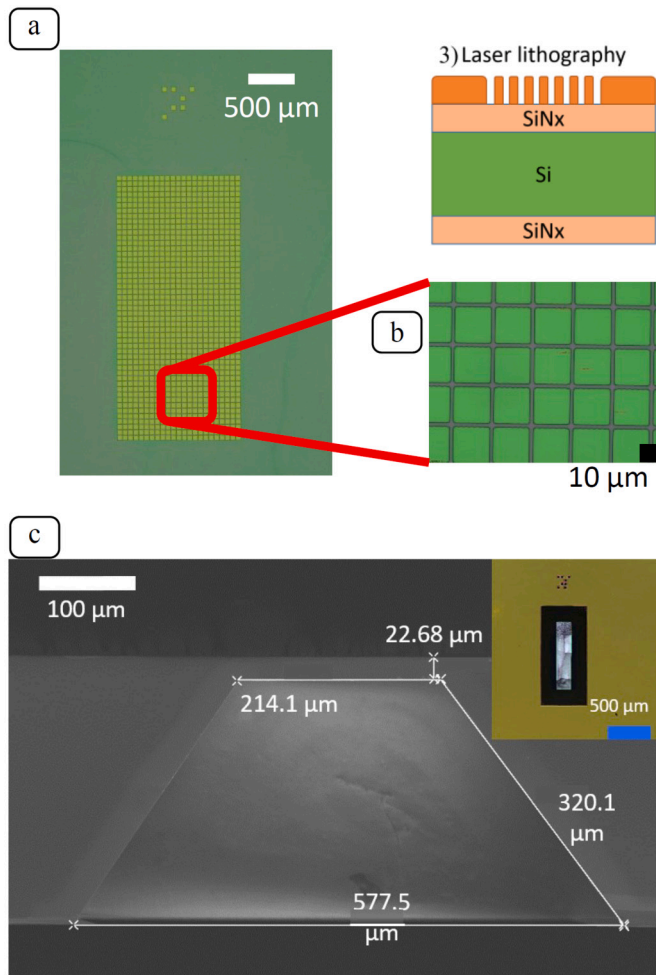


**Fig. 2. Etching mask for back etching.** (a) Photolithography mask that defines a hard mask of  $\text{SiN}_x$  capable of sustaining the subsequent etching of silicon from the bottom surface. The etching solution is made of NaOH at 20% of concentration at  $80^\circ\text{C}$ , at which temperature the etching rate is about  $1.2 \mu\text{m}/\text{min}$ . The silicon is etched along the crystallographic planes  $\langle 100 \rangle$  until a pyramidal shape is formed. Thereafter, the silicon is etched along the  $\langle 111 \rangle$  planes with a slower etch rate because the wet etching is an anisotropic process. (b) Zoomed view of the mesh grid: this pattern delays the etching of silicon so that, at the end, the device is left with around  $20 \mu\text{m}$  of silicon underneath the devices. (c) Cross section of the etched substrate.

the removal of the silicon substrate by submerging the wafer in a solution of  $\geq 85\%$  pure KOH (Sigma Aldrich) at a dilution of 25% in mass at  $60^\circ\text{C}$  (step 22). The remaining silicon is removed by the wet etching, then the device is dipped in IPA to prevent surface tension to collapse the beams (Fig. 4a). Finally, the wafer is lifted above the IPA solution and dried in an enriched IPA vapour environment.

Alternatively, the last suspension process (step 22) can be carried out without the transfer (steps 18–21). In this case, after suspension, a micro positioner was used to transfer a silicon lamella cut from a substrate using focused ion beam. The lamella was fabricated in a FEI Helios Nano Lab 650 microscope operated at 30 kV and 5 kV voltages. To clamp and reduce the contact resistances,  $\sim 150 \text{ nm}$  thick patches of platinum were fabricated using electron beam induced deposition.

## 2.2. Electro-thermal characterization

Electrical measurements were carried out in a 4-wire configuration using four impedance analysers (MFIA Zurich Instruments). During the electrothermal experiments, the device was placed in vacuum to re-

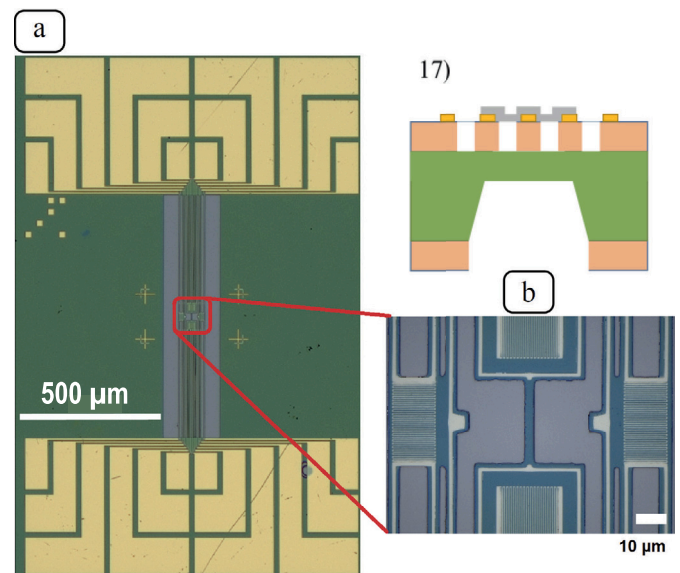


**Fig. 3. Outlook of the device.** (a) Optical image of the whole device, where Au pads and Pt transducers are visible. The yellowish part is the Au layer for the electrodes, the bluish surface in (b) is  $\text{SiN}_x$  on top of silicon and the greyish part in the centre is the exposed silicon after dry etching. (b) Zoomed view of the thermometers: the transducers are made of 3 nm of Cr and 27 nm of Pt.

duce the heat dissipation through convection. We conducted these types of measurements with a vacuum sealed cryostat featuring electrical feedthroughs and an optical window to allow Raman thermometry measurements (CS204SF-DMX-20-OM Closed Cycle Cryostat of Advanced Research Systems). The cryostat cools down the sample using helium in a close-cycle setup. The devices are thermalized to the cryostat temperature, then a constant direct current of 900 nA is applied to the resistor without significantly heating the membranes. For spectroscopy experiments, we used a 532 nm continuous laser (single frequency mode Excelsior) as excitation source, whereas the Raman spectra were acquired using a triple grating (1800 g/mm) spectrometer (HORIBA T64000).

## 3. Results and discussion

### 3.1. Flake suspension

A critical step of the fabrication procedure consists of suspending the device together with the flake. This can lead to contaminations or folding of the layers because of the solution's surface tension. Fig. 4 shows the device after the last step of fabrication. A Raman spectroscopy study is performed to assess the lattice quality before and after the suspension. The inset of Fig. 4b shows the Raman spectrum of a 17 nm thick hBN flake before it is submerged in KOH (shown in black dots), together with the Raman spectrum of the same hBN flake after it is dipped in KOH 20% concentration at a temperature of  $60^\circ\text{C}$  for 1 hour (shown in red dots). The solid lines are the Lorentzian fit of the data. The peaks of the spectra before and after etching are centred around  $1361 \text{ cm}^{-1}$  and have a full width at half maximum of  $10 \text{ cm}^{-1}$  and of  $9 \text{ cm}^{-1}$ , respectively, suggesting that the wet etching process does not damage the lattice structure. Although the surface tension can lead to the folding of graphene layers during the drying process, no hBN flake or graphite broke during the suspension. To prove the general feasibility of the process, besides hBN, we have transferred also graphene and graphite flakes.

### 3.2. Device characterization and calibration

Once the device is fabricated, a series of electrical characterization measurements are performed to calibrate the metal thermometers



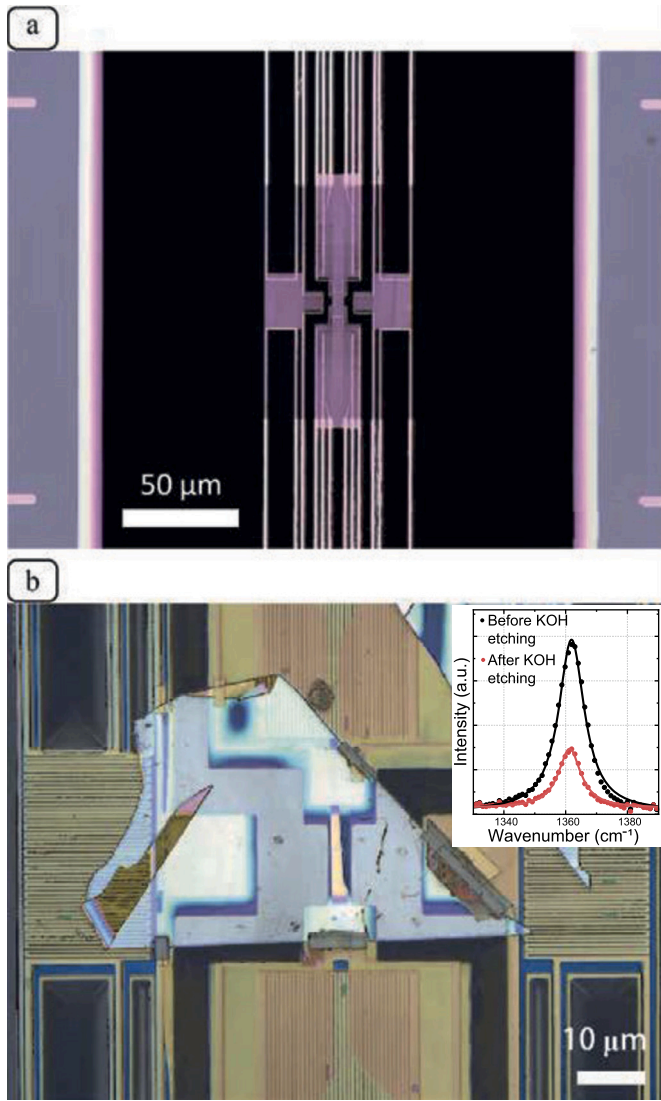


**Fig. 4. Suspended flake.** (a) Fully suspended membranes. (b) A hBN flake is suspended between the four transducers. The flake in this case is clamped between the SiN<sub>x</sub> layer and a Au metal layer on top. The transfer and post-processing of the hBN flake was made in EMPA, Zurich. The inset shows the Raman characterization of a hBN flake before (black dots) and after (red dots) KOH etching. Solid lines are Lorentzian fits of the data. (For interpretation of the colours in the figure(s), the reader is referred to the web version of this article.)

with respect to temperature variations. An accurate characterization of the suspended platforms' thermal dynamics ensures that we acquire the electrical readouts after the system has thermally stabilized. Fig. 5 shows the frequency response of the central platform (the slowest one due to the increased mass), where the third harmonic ( $3\omega$ ) response to an AC excitation of 30  $\mu$ A was studied. From a drop of 10% in the  $3\omega$  potential, we extract a cut-off frequency of 1.6 Hz, indicating that the system requires at least several seconds to fully reach thermal stabilization. Hence, we used 20 s of waiting time for all electronic measurements. The inset of Fig. 5 shows the characteristic cubic current ( $I^3$ ) as a function of the  $3\omega$  signal.

We calibrate the thermometers by measuring the resistances at different background temperatures. A line interpolation of the resistance's values allows to extract the temperature coefficient of resistance (TCR).

$$R = R_0 \cdot (1 + \alpha \cdot \Delta T); \quad \alpha = \frac{1}{R_0} \frac{dR}{dT} \quad (1)$$

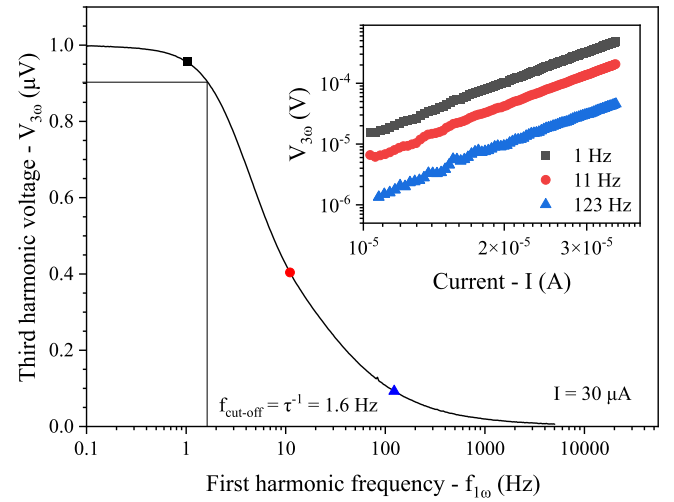


**Fig. 5.  $3\omega$  measurements of the bottom transducer.** Third harmonic voltage signal as a function of the excitation frequency. The solid vertical line highlights the cut-off frequency. The inset illustrates the  $I^3$  dependency of the signal for 3 specific frequencies highlighted in the main chart.

The TCR is proportional to the sensitivity of the thermometers. The driving current at which the resistance starts to heat due to Joule effect is assessed through a series of ramping current. The driving point at which the resistance starts to change is considered the starting heating point. The TCR is assessed by measuring the resistance at 900 nA and varying the cryostat temperature from 50 K to 300 K. The results obtained from a typical device are displayed in Fig. 6. All the transducers display a TCR of  $0.0012 \pm 10^{-5} \text{ K}^{-1}$  at room temperature. Once the TCR is extracted, one of the four resistors of a device can be heated to few Kelvin above the environmental temperature to create a temperature gradient between the membranes by applying a current between 1  $\mu$ A to 7  $\mu$ A.

Importantly, the leakage heat flow that goes from the heater resistor to the sensor resistors may limit the ultimate sensitivity to temperature variation on the sample. A series of tests were performed to extract the parasitic heat current by assessing the cross heating of the membranes in absence of a sample. Fig. 7a shows the left resistor generating a temperature gradient while the top transducer probes the increase in temperature. Fig. 7b shows the bottom resistor generating a temperature gradient, while the top transducer probes the increase in temperature. The left and bottom membranes are separated by a gap and both are connected to the substrate by long beams. The bottom and top membranes are directly connected by a short SiN<sub>x</sub> bridge that leaks the heat power between the two transducers. The SiN<sub>x</sub> bridge is necessary for mechanical stability of the device's centre and to avoid the bending of the top and bottom membranes. The contribution of the SiN<sub>x</sub> bridge is assessed by a test without a sample placed on the device, so that the heat flowing to the bridge can be differentially subtracted from the heat flowing through the sample, when a flake is placed onto the device. The beam conductance from the resistors to the substrate is computed as follows: [10]

$$G_B = \left( \frac{d\Delta T_H}{dP} + \frac{d\Delta T_S}{dP} \right)^{-1} \quad (2)$$

where  $d\Delta T_H$  is the increase in temperature with respect to the background on the heater side, the  $d\Delta T_S$  is the corresponding value for the sensor side, and  $P$  is the total heating power generated by both the transducers plus half of the power from the source and drain beams, Fig. 8. The linear fitting of the rise in temperature with respect to generated power gives the total beam conductance, according to equation (2), which is a characteristic of heat dissipation of the device from the transducers to the substrate through all heat channels. When a side resistor

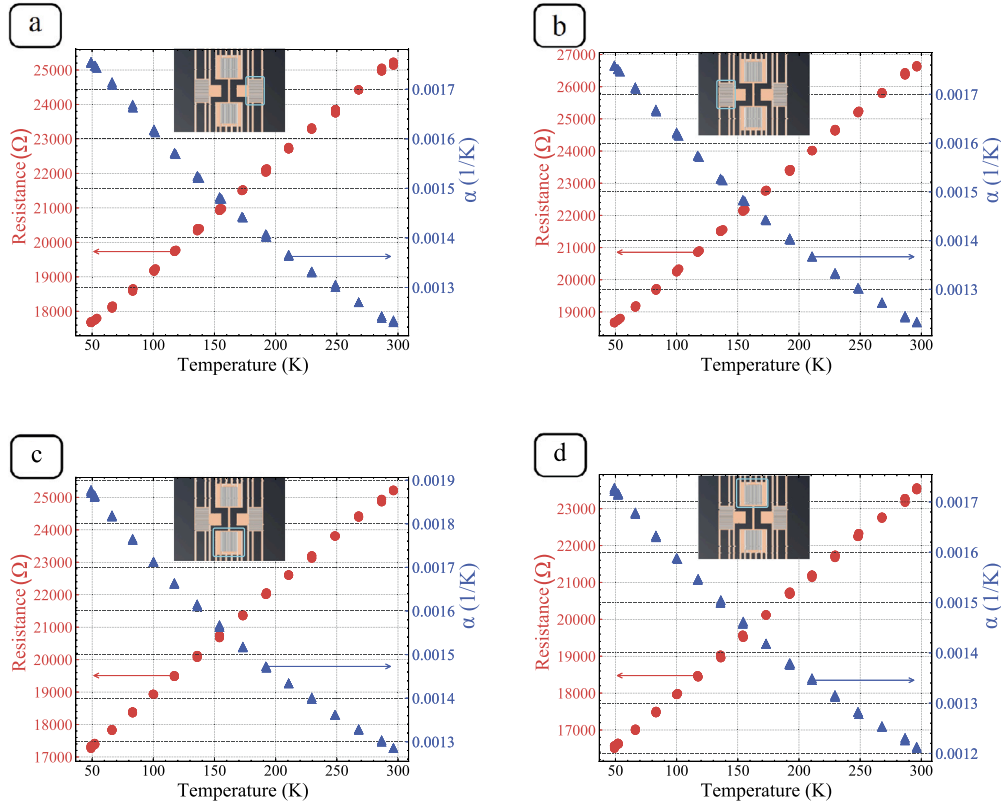


**Fig. 6. Resistance variation of the transducers with respect to temperature.** The electrical resistance of each of the four different transducers is evaluated at different temperatures by using four point measurements to exclude the electrical contact resistance. The temperature coefficient of resistance (TCR) is derived by interpolation and it defines the sensitivity of the resistor to temperature changes. (a) TCR measurement of the right resistor. (b) TCR measurement of the left resistor. (c) TCR measurement of the bottom resistor. (d) TCR measurement of the top resistor.

senses the temperature, the contribution of the sensor in the equation (2) is negligible and the equivalent heat circuit is shown in the inset of Fig. 8a. Fig. 8b illustrates the beam conductance when a central resistor acts as a heater. When one of the side transducer acts as a sensor, the equivalent thermal circuit is shown in inset A Fig. 8b. If the opposite central resistor acts as a sensor, there is a significant contribution in its temperature rise from the heater. The inset B of Fig. 8b depicts the equivalent thermal circuit.

The parasitic heat conductance  $G_P$  is obtained by measuring the relative increase in the resistance of the sensor resistor while the heater generates a heat gradient as in the work of Shi et al. [10]:

$$G_P = G_B \cdot \frac{d\Delta T_S}{dP} \cdot \left( \frac{d\Delta T_H}{dP} - \frac{d\Delta T_S}{dP} \right)^{-1} \quad (3)$$

Using equation (3), the heat cross talk is computed (see Fig. 9). The value refers to all the parasitic processes involved in the device: radiation, conduction, etc. The data relating to the parasitic conductance exhibits a lower limit of sensitivity for the sample on the order of  $10^{-9}$  W/K. Therefore, a heat flows through the flake towards other transducers, the temperature on the remaining membranes is measured with a negligible current thus extracting the temperature drop over the flake. The thermal conductivity of the flake is extracted by dividing the heat flow by the temperature gradient per unit of area.

If one of the side platforms acts as heater, the measurements are noise-dominated as shown in Fig. 9a. If a central platform acts as heater, a negligible heat flow crosses the central membrane to the side membranes, while a not-negligible heat flows through the central bridge as shown in Fig. 9b.

To complete the device characterization, the thermal conductivity of  $\text{SiN}_x$  is obtained as  $k_{\text{SiN}_x} = G_{\text{bridge}} \frac{L}{A}$ , where  $G_{\text{bridge}}$  is the conduc-

tance of the  $\text{SiN}_x$  bridge,  $L$  is the length and  $A$  is the cross-section of the bridge (Fig. 10). When a sample is placed between the top and bottom transducers, the heat circuit can be modelled as a parallel resistance scheme, where part of the heat goes through the bridge and part through the sample. Knowing the thermal conductivity of  $\text{SiN}_x$ , we can subtract the heat going through the bridge from the total heat flow, thus extracting the thermal conductance of the sample.

### 3.3. Estimation of the contact resistance of a silicon lamella

We have transferred through micro-manipulation a monocrystalline silicon lamella to evaluate the impact of the thermal contact resistance and test the sensitivity of the device (Fig. 11a). Since the lamella was prepared by Focused Ion Beam (FIB) cutting, its surface is amorphized, thereby providing a high thermal contact resistance. We have used Raman thermometry to calculate the effective lattice temperature of the lamella as a function of the applied temperature on the membranes. Namely, the phonon frequencies shift with temperature and, therefore, they can be used as lattice thermometer provided that a careful calibration of the frequency shift as a function of temperature has been done. This experiment offers the possibility to explore the impact of dominant thermal contact resistances.

We have increased the left resistor's electrical power to linearly increase the membrane temperature. While measuring the rise of temperature on the other three resistors (right, top, and bottom ones), we have simultaneously measured the lattice temperature of the silicon lamella at a distance of about  $8 \mu\text{m}$  from the edge of the left membrane. Fig. 11a shows the point of measurement highlighted in red. It is worth noticing that the temperature of the lamella, measured by Raman thermometry, increases linearly with the heater power and differs by less than 10 K from the electrically measured heater temperature.

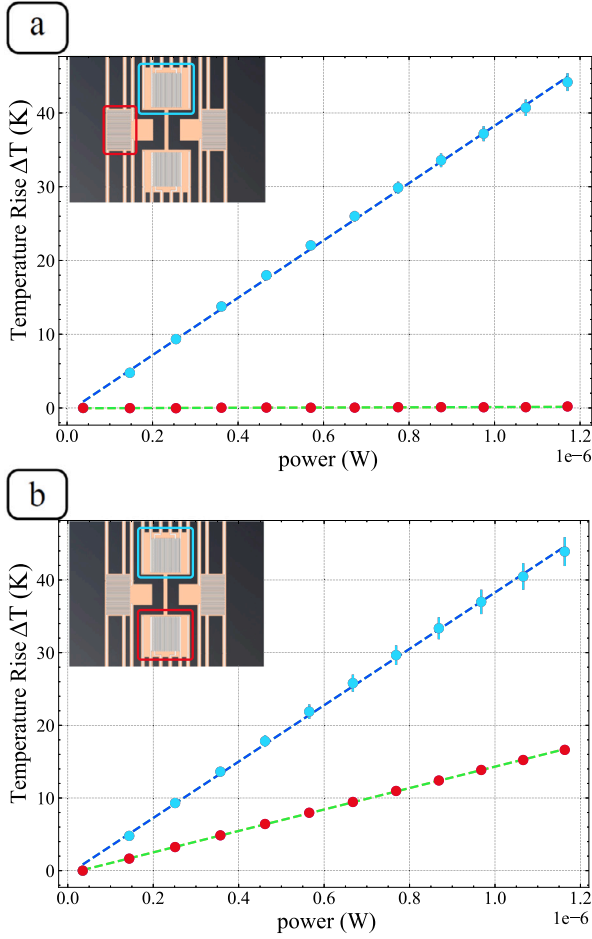


**Fig. 7. Temperature rise with respect to the substrate temperature.** One transducer had the current swept from 0.9  $\mu\text{A}$  up to 7  $\mu\text{A}$  while the other transducer has a low current of 0.9  $\mu\text{A}$  applied to prevent overheating. The resistor with high currents heats up the pads and creates a heat flow towards the other resistor. The heat going through the beams is extracted by linear interpolation of the temperature difference with respect to the total power. The substrate temperature was kept at 103 K. (a) Temperature rise between the left and top transducers. (b) Temperature rise between the bottom and top transducers.

We estimated the thermal contact resistance from the temperature drop between the lamella and the membrane after verifying that the temperature across the lamella was approximately constant, indicating that the thermal transport is contact resistance-dominated. Namely, we have performed Raman thermometry measurements at different distances from the edge of the heated membrane, observing a constant temperature within the measurements' error (bottom chart of Fig. 11a). The absence of a temperature gradient inside the lamella denotes a negligible heat resistance of the sample with respect to the contact resistances of the membranes.

We extracted the interfacial thermal conductances by differentiating the equation of conservation of energy by the total power generated by the heater:

$$G_{CL} = \frac{1 - G_B \cdot \frac{d\Delta T_L}{dP}}{\frac{d\Delta T_L}{dP} - \frac{d\Delta T_{Raman}}{dP}} \quad (4)$$

$$G_{CC} = \frac{G_B \cdot \frac{d\Delta T_T}{dP} + G_B \cdot \frac{d\Delta T_B}{dP}}{\frac{d\Delta T_{Raman}}{dP} - \frac{d\Delta \bar{T}_{br}}{dP}} \quad (5)$$

$$G_{CR} = \frac{G_B \cdot \frac{d\Delta T_R}{dP}}{\frac{d\Delta T_{Raman}}{dP} - \frac{d\Delta T_R}{dP}} \quad (6)$$

where  $G_{CL}$ ,  $G_{CC}$ ,  $G_{CR}$  are the interfacial conductances of the left membrane, central  $\text{SiN}_x$  bridge and right membrane respectively.  $\Delta T_L$ ,  $\Delta T_T$ ,  $\Delta T_B$ ,  $\Delta T_R$  are the temperature rise of the resistors left, top, bottom, right respectively, while  $\Delta T_{Raman}$  is the sample's temperature rise measured through Raman thermometry.  $\Delta \bar{T}_{br}$  is the average temperature rise in the central  $\text{SiN}_x$  bridge and  $w_{bridge}$  is the bridge's width:

$$\frac{d\Delta \bar{T}_{br}}{dP} = \frac{\left( \frac{d\Delta T_T}{dP} + \frac{d\Delta T_B}{dP} \right)}{2} + \frac{G_B \cdot \left( \frac{d\Delta T_T}{dP} + \frac{d\Delta T_B}{dP} \right) \cdot w_{bridge}}{12 \cdot k_{SiN_x}} \quad (7)$$

We assumed that the sample uniformly heats the central  $\text{SiN}_x$  bridge where the two layers are in contact, thus the temperature distribution on the  $\text{SiN}_x$  bridge has a parabolic profile across the area immediately in contact with the lamella. The first term of the equation (7) refers to the first order average, while the second term takes into account the rise in temperature due to the parabolic profile. We computed  $\Delta \bar{T}_{br}$  by spatially integrating the temperature across the sample-bridge contact and dividing it by the contact's length. By differentiating the temperature rise by the power, the offsets cancelled out.

The left membrane displays the lowest interface resistance (Table 1) as it is observed by the small temperature difference between the left heater readout and Raman thermometry on the lamella, Fig. 11b. This is consistent with the greater contact area on the left membrane, Fig. 11a. In contrast, the interface resistances of the central  $\text{SiN}_x$  bridge and the right membrane are higher, as reflected by the larger temperature difference between the lamella and the sensors, Fig. 11b. We extracted the average of the specific interfacial thermal conductance of  $2.4 \pm 0.8 \times 10^4 \text{ W K}^{-1} \text{ m}^{-2}$ . Noteworthy, despite a single contact resistance is calculated for the central bridge, the sensitivity of the top and bottom sensors allows to deduce a clear asymmetry on the contact since the temperature rise is noticeable different at both sides, as it is displayed in the Fig. 11b.

Finally, the aforementioned contact resistances were extracted under the assumption that the temperature of the  $\text{SiN}_x$  underneath the sample is the same as the one recorded by the changes in the electrical resistor. However, it is worth highlighting that this could potentially yield to an error if sufficiently large temperature inhomogeneities arise across the  $\text{SiN}_x$  platform. This effect was studied using a finite element model of the platform. With this model, the relative temperature inhomogeneity across the  $\text{SiN}_x$  ( $\Delta T_{error}$ ) with respect to the total temperature rise is calculated as a function of a sink conductance ( $G_{sink}$ ), which accounts for the conductance of the sample in series with the rest of the platform beam conductance:

$$\Delta T_{error} = \frac{(T_{heater} - T_{underneath})}{(T_{heater} - T_{bulk})}$$

The normalized error as a function of  $G_{sink}$  only reaches 1.8% in the limit of the physically possible range. Namely, the error reaches this maximum value in the limit of the sink conductance approaching the value of the beam conductance of the adjacent platform and beams ( $10\text{--}20 \times 10^8 \text{ W/K}$ ).

#### 4. Conclusion

In this article, we presented a suspended micro electro-mechanical device composed of four platinum thermometers. The sample to study is inserted into a cryostat to control the background temperature; an optical window on top is used to shine a laser and performing Raman thermometry, while the bonding pads allow to electrically heat the transducers. The device is capable of measuring the heat flow in

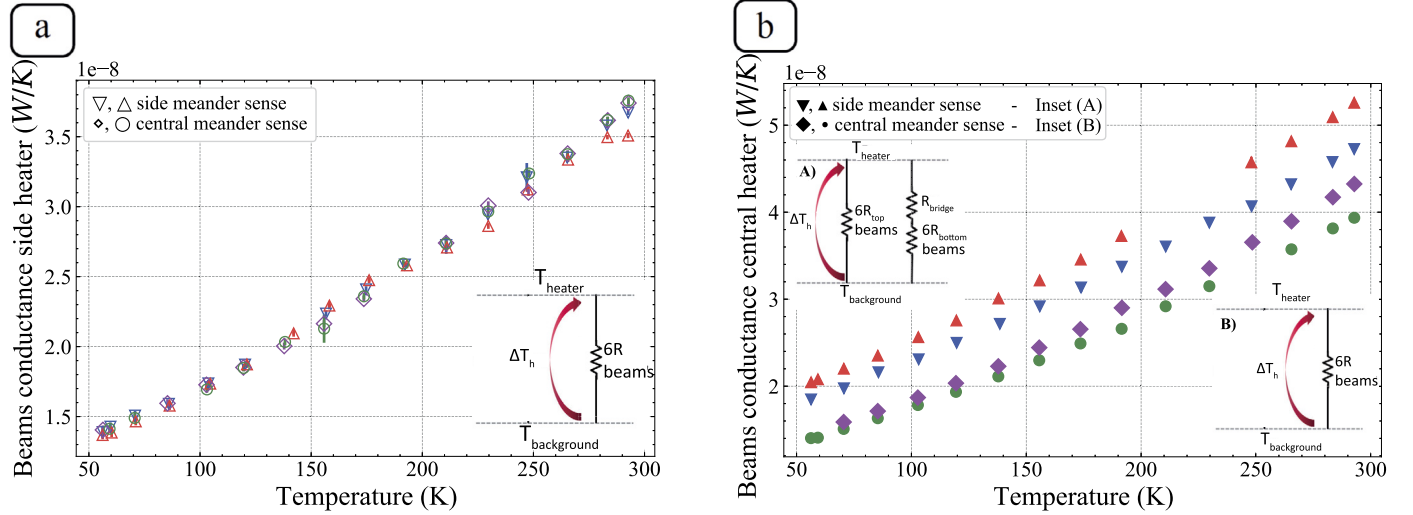


**Fig. 8. Beams heat conductance.** Panel (a) shows the total beam conductance when one of the side resistor acts as a heater, in this case all the power is dissipated through the 6 beams of the heater. Panel (b) shows the total beam conductance when one of the central resistors is the heater. Inset A) and B) represent the equivalent circuit when sensing the temperature with a side resistor or a central resistor respectively.

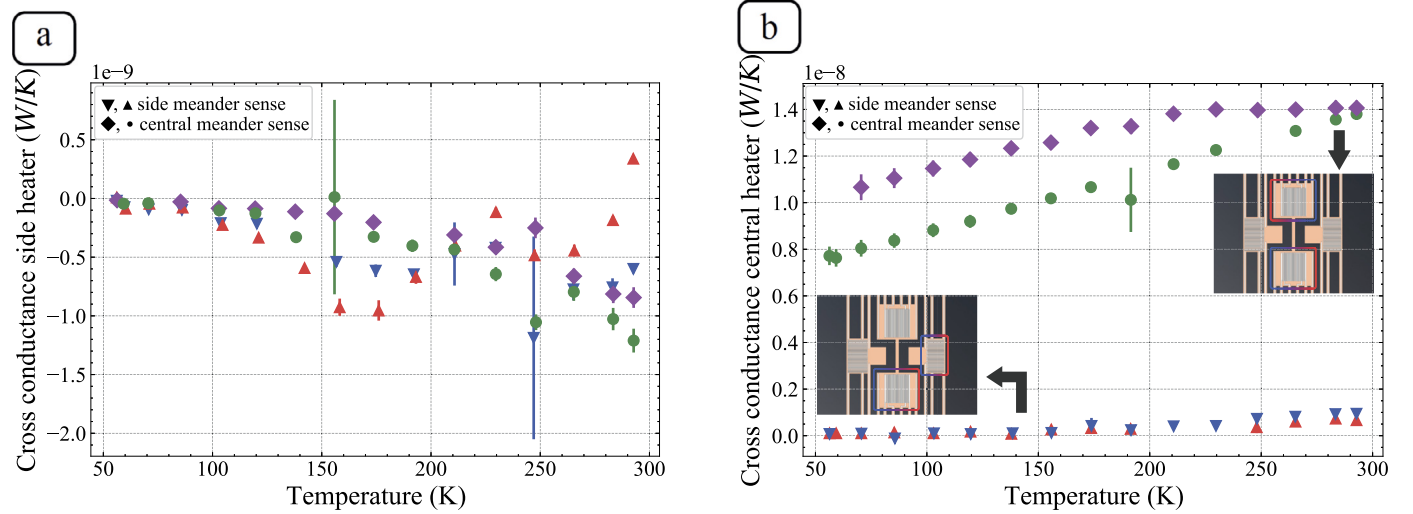


**Fig. 9. Parasitic heat conductance.** The device's heat cross talk is extracted by heating up one resistor and sensing the temperature variation in the other membrane without a sample bridging the resistors. (a) Parasitic heat conductance, when one of the side resistor is heating (right/left). (b) Parasitic heat conductance, when one of the central resistor is heating (top/bottom).

**Table 1**  
Interfacial thermal conductances.

	Left membrane	Central SiN <sub>x</sub> bridge	Right membrane
Total interfacial conductance W/K	$6.51 \times 10^{-7}$	$1.16 \times 10^{-7}$	$1.01 \times 10^{-7}$
Specific interfacial conductance W/Km <sup>2</sup>	$4.34 \times 10^4$	$8.8 \times 10^3$	$2.03 \times 10^4$

more than one direction, hence this spacial sensitivity allows to extract the anisotropic thermal properties of a material of interest and perform a fully electrical and optical characterization. The substrate is etched to provide a throughout optical access from below the sample and isolate it from background conduction, thus, increasing the sensitivity of the experiments. The final suspension of the device together with a hBN layer remains a challenging part of the fabrication, but it was proven that the process does not significantly alter the lattice structure of the flake. This kind of transfer and suspension may also be employed in

a stack of hBN, graphene, and hBN. The working principles of the device are shown, as well as the minimum sensitivity in a temperature range between 50 K to 300 K. Finally, we validated the accuracy of the device using a 250 nm thick silicon lamella and Raman thermometry to calculate the effective lattice temperature of the lamella as a function of the applied temperature on the membranes. Raman measurements revealed a contact-resistance dominated heat regime where the temperature across the lamella is homogeneous. The spatial sensitivity of the device enables the extraction of the different individual



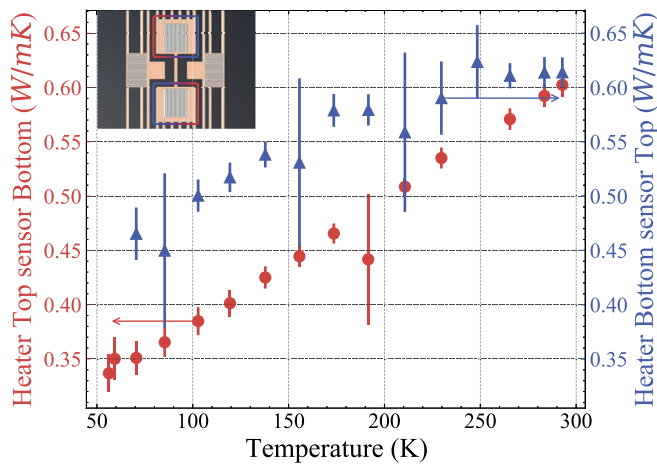


**Fig. 10. SiN<sub>x</sub> thermal conductivity.** The thermal conductivity of the SiN<sub>x</sub> layer is extracted from the heat cross talk of the top and bottom platforms. The heat conductance flowing across the top and bottom platforms, through the SiN<sub>x</sub>, is divided by the cross section of the bridge and multiplied by its length to extract the thermal conductivity of the SiN<sub>x</sub> layer.

contact resistances, with an average interfacial thermal conductance of  $2.4 \pm 0.8 \times 10^4 \text{ WK}^{-1} \text{ m}^{-2}$ .

#### CRediT authorship contribution statement

**G. de Vito:** Writing – original draft, Validation, Software, Methodology, Investigation, Conceptualization. **D.M. Koch:** Writing – review & editing, Methodology, Investigation. **G. Raciti:** Writing – review & editing, Validation, Investigation. **J.M. Sojo-Gordillo:** Writing – original draft, Visualization, Software, Formal analysis. **A. Nigro:** Writing – review & editing, Methodology, Investigation, Conceptualization. **R. Swami:** Writing – review & editing, Methodology. **Y. Kaur:** Validation, Methodology. **M.Y. Swinkels:** Writing – review & editing, Validation, Methodology. **W. Huang:** Validation, Methodology. **T. Paul:** Writing – review & editing, Validation, Methodology. **M. Calame:** Writing – review & editing, Supervision, Funding acquisition. **I. Zardo:** Writing – original draft, Supervision, Resources, Project administration, Funding acquisition, Conceptualization.

#### Declaration of competing interest

There are no conflicts to declare.

#### Data availability

The data that support the findings of this study are openly available in [Four Terminal Suspended Thermal Bridge](#), reference number 10635934.

#### Acknowledgement

This project has received funding from the Swiss National Science Foundation grant (Grant No. 189924, Hydronics) and from the European Research Council (ERC) under the European Union's Horizon 2020 research and innovation program (grant agreement No. 756365). GR acknowledges financial support also through Eucor, The European Campus (Marie Skłodowska-Curie grant agreement number 847471). We also acknowledge Dr. Gerard Gadea for his assistance in fabrication process as well as the mechanical workshop and electrical workshop of the Department of Physics of the University of Basel.

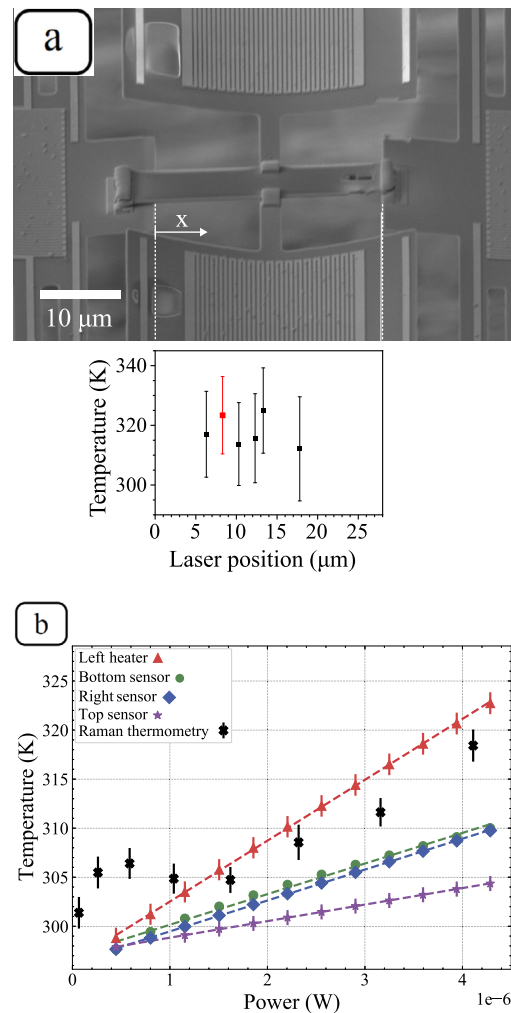


**Fig. 11. Silicon lamella, thermometry experiment.** (a) A FIB cut silicon lamella of  $38 \mu\text{m} \times 5 \mu\text{m} \times 250 \text{nm}$  is transferred onto an already suspended device using micromanipulators. We used Raman thermometry to map the temperature distribution of the sample, reported in the bottom chart. The measurements were performed keeping the left resistor at a constant temperature of 363.5 K to generate a heat gradient. (b) Electrically measured temperature of the heater (red triangles), and the three sensors (spheres, diamonds, and stars) as a function of heating power. The black crosses are the temperature of the lamella measured by Raman thermometry at a distance of about  $8 \mu\text{m}$  from the edge of the left membrane.

#### References

- [1] A.A. Balandin, Thermal properties of graphene and nanostructured carbon materials, *Nat. Mater.* 10 (8) (2011) 569–581, <https://doi.org/10.1038/nmat3064>, <https://www.nature.com/articles/nmat3064>.
- [2] S. Gomès, A. Assy, P.O. Chapuis, Scanning thermal microscopy: a review, *Phys. Status Solidi A* 212 (3) (2015) 477–494, <https://doi.org/10.1002/PSSA.201400360>, <https://onlinelibrary.wiley.com/doi/full/10.1002/pssa.201400360>.
- [3] D. Buckley, Z.R. Kudrynskiy, N. Balakrishnan, T. Vincent, D. Mazumder, E. Castanon, Z.D. Kovalyuk, O. Kolosov, O. Kazakova, A. Tzalenchuk, A. Patané, D. Buckley, T. Vincent, E. Castanon, O. Kazakova, A. Tzalenchuk, Z.R. Kudrynskiy, D. Mazumder, A. Patané, N. Balakrishnan, Z.D. Kovalyuk, C. Branch, U.O. Kolosov, Anomalous low thermal conductivity of atomically thin InSe probed by scanning thermal microscopy, *Adv. Funct. Mater.* 31 (11) (2021) 2008967, <https://doi.org/10.1002/ADFM.202008967>, <https://onlinelibrary.wiley.com/doi/full/10.1002/adfm.202008967>.
- [4] S. Gonzalez-Munoz, K. Agarwal, E.G. Castanon, Z.R. Kudrynskiy, Z.D. Kovalyuk, J. Spìeço, O. Kazakova, A. Patané, O.V. Kolosov, Direct measurements of anisotropic thermal transport in  $\gamma$ -InSe nanolayers via cross-sectional scanning thermal microscopy, *Adv. Mater. Interfaces* 10 (17) (2023) 2300081, <https://doi.org/10.1002/ADMI.202300081>, <https://onlinelibrary.wiley.com/doi/full/10.1002/admi.202300081>.

- [5] A. Weathers, L. Shi, Thermal transport measurement techniques for nanowires and nanotubes, *Annu. Rev. Heat Transf.* 16 (1) (2015) 101–134, <https://doi.org/10.1615/AnnualRevHeatTransfer.v16.40>, arXiv:1504.05128v1, <http://arxiv.org/abs/1504.05128>.
- [6] A. Weathers, K. Bi, M.T. Pettes, L. Shi, Reexamination of thermal transport measurements of a low-thermal conductance nanowire with a suspended micro-device, *Rev. Sci. Instrum.* 84 (8) (2013) 084903, <https://doi.org/10.1063/1.4816647>, <https://aip.scitation.org/doi/abs/10.1063/1.3532848>.
- [7] M. Soini, I. Zardo, E. Uccelli, S. Funk, G. Koblmüller, A. Fontcuberta, I. Morral, G. Abstreiter, Thermal conductivity of GaAs nanowires studied by micro-Raman spectroscopy combined with laser heating, *Appl. Phys. Lett.* 97 (26) (2010) 263107, <https://doi.org/10.1063/1.3532848>.
- [8] O. Braun, R. Furrer, P. Butti, K. Thodkar, I. Shorubalko, I. Zardo, M. Calame, M.L. Perrin, Spatially mapping thermal transport in graphene by an opto-thermal method, *npj 2D Mater. Appl.* 6 (1) (2022) 1–7, <https://doi.org/10.1038/s41699-021-00277-2>, <https://www.nature.com/articles/s41699-021-00277-2>, 2022.
- [9] X. Liu, X. Wu, T. Ren, In situ and noncontact measurement of silicon membrane thermal conductivity, *Appl. Phys. Lett.* 98 (17) (2011) 174104, <https://doi.org/10.1063/1.3583603/908378>.
- [10] L. Shi, D. Li, C. Yu, W. Jang, D. Kim, Z. Yao, P. Kim, A. Majumdar, Measuring thermal and thermoelectric properties of one-dimensional nanostructures using a microfabricated device, *J. Heat Transf.* 125 (5) (2003) 881–888, <https://doi.org/10.1115/1.1597619>.
- [11] P. Kim, L. Shi, A. Majumdar, P.L. McEuen, Thermal transport measurements of individual multiwalled nanotubes, *Phys. Rev. Lett.* 87 (21) (2001) 215502, <https://doi.org/10.1103/PhysRevLett.87.215502>, arXiv:cond-mat/0106578v1.
- [12] M.Y. Swinkels, I. Zardo, Nanowires for heat conversion, <https://doi.org/10.1088/1361-6463/aad25f>, jul 2018, <https://iopscience.iop.org/article/10.1088/1361-6463/aad25f>.
- [13] X. Huang, Y. Guo, Y. Wu, S. Masubuchi, K. Watanabe, T. Taniguchi, Z. Zhang, S. Volz, T. Machida, M. Nomura, Observation of phonon Poiseuille flow in isotopically-purified graphite ribbons, <http://arxiv.org/abs/2207.01469>, jul 2022.
- [14] R. Anufriev, Y. Wu, M. Nomura, Ballistic heat conduction in semiconductor nanowires, *J. Appl. Phys.* 130 (7) (2021) 70903, <https://doi.org/10.1063/5.0060026/1061462>.
- [15] A. Tavakoli, J. Maire, B. Brisuda, T. Crozes, J.F. Motte, L. Saminadayar, E. Collin, O. Bourgeois, Experimental evaluation of thermal rectification in a ballistic nanobeam with asymmetric mass gradient, *Sci. Rep.* 12 (1) (2022) 1–7, <https://doi.org/10.1038/s41598-022-11878-2>, <https://www.nature.com/articles/s41598-022-11878-2>.
- [16] J. Maire, R. Anufriev, M. Nomura, Ballistic thermal transport in silicon nanowires, *Sci. Rep.* 7 (1) (2017) 1–8, <https://doi.org/10.1038/srep41794>, <https://www.nature.com/articles/srep41794>.
- [17] S.F. Karg, V. Troncale, U. Drechsler, P. Mensch, P. Das Kanungo, H. Schmid, V. Schmidt, L. Gignac, H. Riel, B. Gotsmann, Full thermoelectric characterization of InAs nanowires using MEMS heater/sensors, *Nanotechnology* 25 (30) (2014) 305702, <https://doi.org/10.1088/0957-4484/25/30/305702>, <https://iopscience.iop.org/article/10.1088/0957-4484/25/30/305702>.
- [18] J. Kim, E. Ou, D.P. Sellan, L. Shi, A four-probe thermal transport measurement method for nanostructures, *Rev. Sci. Instrum.* 86 (4) (2015) 044901, <https://doi.org/10.1063/1.4916547>, <https://aip.scitation.org/doi/abs/10.1063/1.4916547>.
- [19] J. Gooth, F. Menges, N. Kumar, V. Süß, C. Shekhar, Y. Sun, U. Drechsler, R. Zierold, C. Felser, B. Gotsmann, Thermal and electrical signatures of a hydrodynamic electron fluid in tungsten diphosphide, *Nat. Commun.* 9 (1) (2018) 1–8, <https://doi.org/10.1038/s41467-018-06688-y>, <https://www.nature.com/articles/s41467-018-06688-y>.
- [20] K. Hippalgaonkar, B. Huang, R. Chen, K. Sawyer, P. Ercius, A. Majumdar, Fabrication of microdevices with integrated nanowires for investigating low-dimensional phonon transport, *Nano Lett.* 10 (11) (2010) 4341–4348, <https://pubs.acs.org/doi/full/10.1021/nl101671r>.
- [21] R. Anufriev, S. Gluchko, S. Volz, M. Nomura, Probing ballistic thermal conduction in segmented silicon nanowires, *Nanoscale* 11 (28) (2019) 13407–13414, <https://doi.org/10.1039/C9NR03863A>, <https://pubs.rsc.org/en/content/articlehtml/2019/nr/c9nr03863a>.
- [22] A. Tavakoli, K. Lulla, T. Crozes, N. Mingo, E. Collin, O. Bourgeois, Heat conduction measurements in ballistic 1D phonon waveguides indicate breakdown of the thermal conductance quantization, *Nat. Commun.* 9 (1) (2018) 1–8, <https://doi.org/10.1038/s41467-018-06791-0>, <https://www.nature.com/articles/s41467-018-06791-0>.
- [23] E.S. Kim, R.S. Muller, R.S. Hijab, Front-to-backside alignment using resist-patterned etch control and one etching step, *J. Microelectromech. Syst.* 1 (2) (1992) 95–99, <https://doi.org/10.1109/84.157364>, <https://ieeexplore.ieee.org/document/157364>.
- [24] L. Wang, I. Meric, P.Y. Huang, Q. Gao, Y. Gao, H. Tran, T. Taniguchi, K. Watanabe, L.M. Campos, D.A. Muller, J. Guo, P. Kim, J. Hone, K.L. Shepard, C.R. Dean, One-dimensional electrical contact to a two-dimensional material, *Science* 342 (6158) (2013) 614–617, <https://doi.org/10.1126/science.1244358>, <https://www.science.org/doi/10.1126/science.1244358>.